Neuro-Oncology Advances
7(1), vdaf055, 2025 | https://doi.org/10.1093/noajnl/vdaf055 | Advance Access date 6 March 2025

Heterogeneity of intracellular calcium signaling of glioblastoma cells depends on intratumoral location and migration state

Vinoshene Pillai, Enrico Pracucci, Francesco Trovato, Riccardo Parra, Silvia Landi†, and Gian Michele Ratto†

All author affiliations are listed at the end of the article
†These authors are joint last authors.

Corresponding Authors: Vinoshene Pillai, PhD, Institute of Neuroscience CNR, via G. Moruzzi 1, 56124 Pisa, Italy (vinoshene.pillai@gmail.com); Gian Michele Ratto, PhD, Institute of Biophysics CNR, via G. Moruzzi 1, 56124 Pisa, Italy (gianmichele.ratto@sns.it).

Abstract

Background. Glioblastoma (GB), is an incurable brain tumor characterized by extreme malignancy and invasiveness, and the cellular mechanisms underlying such a severe phenotype are not completely understood. Although calcium (Ca^{2+}) plays an important part in tumor proliferation and infiltration, it remains unclear whether Ca^{2+} signaling in GB cells is related to its location within the tumor and on the infiltrative potential of the cells.

Methods. In this study, we developed a stably transfected GL261 cell line that coexpresses a red fluorescent protein for actin cytoskeleton staining and the intracellular Ca^{2+} sensor, GCaMP6s. By means of intravital 2-photon imaging, we have characterized the morphological and functional properties of cells at different locations within the tumor.

Results. Our results showed that cells located at the tumor core are densely packed and rounded in shape, contrasting sharply with the polarized morphology observed in the peripheral cells. This anatomical heterogeneity corresponded to notable variations of the physiological phenotype: cells at the tumor core displayed low Ca^{2+} activity and very limited motility, while peripheral cells displayed intense Ca^{2+} activity and increased migration rates. Moreover, peripheral cells formed a cellular ensemble characterized by synchronized Ca^{2+} activity accompanied by a directionally biased collective motility.

Conclusions. These findings suggest that GB cells manifest activity patterns depending upon their spatial location within the tumor and that these correlate with their migration.

Key Points

- Interplay of Ca^{2+} dynamics and cell motility in GB is crucial.
- GB forms cooperative networks, communicating via Ca^{2+} transients.
- Uncovering Ca^{2+} signaling mechanisms in GB is vital for potential therapy.

Glioblastoma (GB) stands out as one of the most aggressive forms of brain tumor with an unfavorable prognosis.[1,2] The ability of GB to infiltrate brain tissue several centimeters away from the mass highlights the aggressive nature of the disease.[3] This feature of GB is primarily responsible for recurrence and treatment resistance.[4] The presence of tumor microenvironment plays a crucial role in supporting GB infiltration by facilitating the formation of multicellular tumor networks through signaling pathways, gap junctions, and microtubules.[5,6]

Currently, there are several evidences showing that GB cells, both murine and human cell lines, establish connections

Importance of the Study

Our research highlights the intricate relationship between intracellular calcium dynamics and cellular movement in glioblastoma (GB), underscoring the importance of intratumoral signaling in tumor progression. Future investigations should aim to uncover the molecular mechanisms behind calcium signaling in GB and assess its potential for therapy. Targeting abnormal calcium activity could be a promising approach to hinder GB invasion and enhance patient outcomes.

among themselves forming cooperative networks, particularly via gap junctions, and communicate using calcium (Ca^{2+}) waves.[7–11] Many cellular functions such as energy transduction, apoptosis, chemotaxis, and most part of the signal transduction pathways operating within the brain are regulated by Ca^{2+}.[12–14] These functions are triggered by Ca^{2+} redistribution between the cytosol and both intracellular compartments and extracellular space, resulting in Ca^{2+} transients with diverse temporal and spatial features.[15–17] Since GB is characterized by a large degree of intratumor heterogeneity,[18] we should ask whether intracellular Ca^{2+} signaling is uniform within the tumor mass or if different regions of the tumor sustain distinct patterns of Ca^{2+} activity.

The importance of Ca^{2+} signaling extends beyond normal physiological functions in the brain to the regulation of tumor biology, especially in malignancies like GB.[19,20] Dysregulated Ca^{2+} signaling is a hallmark of cancer progression, with GB cells exploiting Ca^{2+}-dependent pathways to enhance their invasiveness and treatment resistance.[20] For instance, low-voltage-activated T-type Ca^{2+} channels (Cav3.1 and Cav3.2) have been shown to regulate critical processes such as cell cycle and survival in GB cells.[21,22] Studies have demonstrated that inhibiting these channels can reduce GB proliferation and induce apoptosis.[23,24] Furthermore, transient receptor potential (TRP) channels, particularly TRPV1 and TRPV2, are implicated in GB cell chemoresistance and tumor progression, suggesting that targeting Ca^{2+} channels may offer therapeutic benefit.[25–28]These findings underscore the potential of Ca^{2+} signaling as a therapeutic target for overcoming the limitations of conventional treatments like temozolomide and radiation therapy.

Building on these insights, several therapeutic strategies are currently being investigated in clinical trials, focusing on modulating Ca^{2+} signaling pathways in GB. For example, clinical trials involving T-type Ca^{2+} channel inhibitors like mibefradil have shown encouraging results when used in combination with standard chemotherapeutics.[29] Other approaches include targeting SERCA pumps and specific Ca^{2+} transport proteins, aiming to disrupt Ca^{2+} homeostasis in GB cells.[30–35]The modulation of Ca^{2+} signaling could induce cytotoxic calcium overload, driving apoptosis and improving therapeutic outcomes. These advances highlight the growing recognition of Ca^{2+} signaling as a crucial target for novel GB therapies and emphasize the need for further research to develop more effective, personalized treatments.

This study aims to investigate the heterogeneity of intracellular Ca^{2+} ($[Ca^{2+}]_i$) activity within different GB districts and the association with invasiveness. To achieve this, we developed a fluorescent GL261 mouse model engineered to express a genetically encoded calcium sensor, GCaMP6s. Taking advantage of *in vivo* 2-photon microscopy, we assessed the $[Ca^{2+}]_i$ dynamics of cells in different tumor areas as the transplanted cells colonize the host brain. Our study reveals differential $[Ca^{2+}]_i$ activity between the tumor core (TC) and peritumoral region, corresponding to large morphological differences and migratory potential of these cells. These findings enhance our understanding of GB complexity.

Materials and Methods

Plasmid

A stably transfected GL261 cell line was produced from pPBC-G6s plasmid, which was kindly donated to us by Karen Wilcox (University of Utah). pBC-G6s is based on a pSP72 backbone, and it expresses calcium sensor GCaMP6s under the constitutive promoter CAG. The GCaMP6s gene, together with the promoter, is flanked by *piggyBac* ITRs, which allow its insertion in a target cell genome in the presence of the helper plasmid, *piggyBac* transposase (PBase). We modified this plasmid by adding at the C-terminal of GCaMP6s an auto-cleavable linker P2A, followed by the red fluorescent protein (RFP) DsRed2, which was modified by adding an N-terminal actin-staining peptide (LifeAct). The RFP was added using a standard digestion-ligation procedure, by using pBC-G6s as a vector and inserting the LifeAct-RFP from a custom plasmid synthesized by a gene synthesis facility (Aurogene), using PstI and NotI restriction enzymes. The subsequent final structure was used in all experiments of the GL261 model. Transformations have been performed in One Shot Stbl3 chemically competent *Escherichia coli* cell line (Thermo Fisher Scientific), while the final plasmid used for transfection was produced using the QIAGEN Plasmid Plus Maxi Kit.

Cell Culture Transfection

GL261 wild-type (GL261-WT) cell line was given to us by Matteo Caleo, CNR Pisa. Cells were cultured in Dulbecco's modified Eagle's medium (Gibco) containing 10% fetal bovine serum, 1% penicillin-streptomycin (100 units/mL of penicillin and 100 µg/mL of streptomycin, Gibco), 1 mM sodium pyruvate (Gibco), and 10 mM 4-(2-hydroxyethyl)-1-piperazineethanesulfonic acid (HEPES) (Gibco). Transfections were performed through electroporation on cell suspension. Cells cultured on P60 Petri dishes (60 mm

diameter) at 80% confluency were detached using 0.05% Trypsin-Ethylenediaminetetraacetic acid (EDTA) (Gibco), washed with 5 mL of Dulbecco's Phosphate-Buffered Saline (PBS), and centrifuged at 1200 rpm for 5 min. Pelleted cells were resuspended in 120 µL of electrolytic buffer (Invitrogen) with 5 µL of plasmid DNA. Resuspended cells were electroporated using MicroPorator MP-100 (Digital Bio, 2 pulses at 1200V with a duration of 20 ms). The amount of DNA used is approximately 10-20 µg. Transfected cells (GL261-TF) were then plated and maintained in the prepared culture medium, replaced 2-3 times per week, in a humidified atmosphere of 5% CO_2 at 37°C. To achieve a 100% stably transfected fluorescent cell line, electroporated cells were sorted using Bio-Rad S3e Cell Sorter. For injection, sorted cells were grown up to 90% confluency in a P60 Petri dish and harvested using 0.05% Trypsin-EDTA. Cells were then pelleted by centrifugation at 1200 rpm for 5 min and resuspended to a cell concentration of 20 000 cells/µL with PBS.

Cell Proliferation Assay

GL261 cells (GL261-WT and GL261-TF) were detached using 0.05% Trypsin-EDTA (Gibco), washed with culture medium, centrifuged at 1200 rpm for 5 min, and resuspended with culture medium. Centrifugation was done to minimize the number of dead cells and cell debris. Then, 10 µL of cell suspension was added to 10 µL of Trypan Blue stain 0.4% (Invitrogen) and loaded into cell counting chamber slides (Invitrogen). Counts were performed using the benchtop Countess Automated Cell Counter (Invitrogen). Cells were seeded on a P60 Petri dish at a starting density of 1×10^4 cells. Cells were detached and counted using the automated cell counter for a period of 6 days, where one Petri dish per day was used (6 Petri dishes/cell line each trial). A total of 3 trials were done.

Wound Healing Assay

In vitro cell migration assay was done by preparing cell suspension in culture medium and counting the cells as described in 3.4.3. Cell suspension then was adjusted to a cell concentration of 4×10^5 cells/mL to obtain a confluent cell layer after 24 h. About 70 µL of cell suspension was applied to each well of the Culture-Insert Well (Ibidi) that was placed in a P35 Petri dish (35 mm diameter) and incubated at 37°C in 5% CO_2 for 24 h. Once a confluent layer is formed, the Culture-Insert Well was gently removed with sterile tweezers. Petri dish was then washed and filled with fresh culture medium to remove dead cells, nonattached cells, and cell debris. Cells were imaged with a Zeiss LSM-800 Airyscan confocal microscope under brightfield mode. Images were acquired using a 20× air objective (NA 0.5) for 2-3 consecutive days until gap closure. Images are at a resolution of 1024 × 1024 pixels, with a field of about 638.9 µm and a linear pixel size of 0.624 µm per pixel.

Animals

C57BL6/J mice strain were obtained from The Jackson Laboratory (stock number #000664) and maintained at Istituto di Neuroscienze (CNR, Pisa) animal house on a 12-h light cycle and fed ad libitum. For all experiments, mice of either sex were studied unless stated otherwise. All animal care and experimental procedures were in strict accordance with standards set by the institutional animal care and the recommendations of the Italian Ministry of Health (protocol 143-2017 PR).

Intracortical Injections of GL261 Cell Line

Mice were anesthetized with 2,2,2-tribromoethanol (Avertin) (0.02 mL/g body weight) intraperitoneally and mounted on a stereotactic stage. The head was secured using 2 metal ear bars and a nose clamp. The hair on the head was removed using a hair depilatory cream, and a single skin cut of approximately 0.5-1 cm was made using a pair of scissors, and the exposed subcutaneous tissue was gently removed. A small needle-size hole around the visual area was made using a hand drill and washed with a few drops of PBS to clean the injection area. Next, 4×10^4 GL261 cells suspended in 2 µL of PBS were injected stereotactically using a glass capillary in the middle of the drilled grove at a depth of 0.3 mm. A total of 5 min were spent for the injection and an additional 2 min before removing the glass capillary to avoid spillovers. The surface of the injection site was then washed with PBS before closing the skin with simple stitches. Iodine antiseptic cream was applied on the stitches to prevent infection. A single dose of antipyretic, that is, 5 drops of paracetamol (100 mg/mL) per 100 mL of drinking water was provided for the animals after surgery. Mice were closely monitored for behavior, reactivity, and appearance.

Survival Analysis

C57BL6/J mice were divided into 2 groups and implanted with tumor cells, GL261-WT, and GLL261-TF, respectively (6 mice/group). Tumor implantation was carried as previously described. Animals were maintained on a 12-h light cycle and fed ad libitum. Animals were closely monitored, and body weights were recorded daily. The endpoint of the experimental duration is achieved when the mice have reduced 20% of its initial body weight. All animals were sacrificed with an overdose of anesthesia at the end of the experiment.

Cranial Window Surgery

Cranial window surgeries were performed from 7 to 28 days post tumor implantation taking into account evidences of symptomatic timeline post GL261 injection from a previous study.[36] Mice were anesthetized with Avertin (0.02 mL/10 g) and mounted on a stereotactic stage. During the experiment, the body temperature of mice was monitored and held constant at 37°C with a feedback-controlled heating blanket (Harvard Instruments). Using a pair of scissors, a longitudinal incision of the skin was performed between the occiput and the forehead, followed by skin and subcutaneous tissue removal around the injected site. A custom-made steel head post with a central imaging

chamber was then glued with cyanoacrylate in a plane approximately parallel with the skull over the cortical region of interest and cemented in place with white dental cement (Paladur). Using a hand drill, the skull was thinned to open a 5 mm diameter window. Forceps were used to break and remove the skull gently. The dura mater was continuously rinsed with sterile artificial cerebrospinal fluid (126 mM NaCl, 26 mM $NaHCO_3$, 1.3 mM $MgSO_4$, 3 mM KCl, 1.25 KH_2PO_4, 2.4 mM $CaCl_2$, 15 mM glucose, and 1.2 mM HEPES in distilled H_2O, pH 7.4). A 5 mm cover glass was used to cover the craniotomy and secured with cyanoacrylate glue.

In vivo 2-Photon Microscopy

High-resolution *in vivo* imaging was performed with a Prairie Ultima Multiphoton microscope (Bruker) equipped with a mode-locked Ti: Sapphire laser (Chameleon Ultra II, Coherent) through a 20X Olympus XLUMPLFLN water immersion objective (numerical aperture 1.0). The power at the sample surface during acquisitions was maintained under 50 mW. Fluorescent cells were imaged at various depths in the cortex. All imaging experiments were performed at the excitation wavelength of 980 nm. This wavelength was chosen for 2 reasons: 1. to be able to excite both GCaMP6s and LifeAct-DsRed2; 2. to enable acquisitions into deeper cortical tissue since the presence of malignant cells increases tissue scattering. The emission filters bandpass used were 490-560 nm for the green channel and 584-680 nm for the red channel. Time-lapse imaging of 10 min was acquired at a resolution of 512 × 512 pixels at zoom 2, leading to a field of about 304.1 µm and a linear resolution of 0.59 µm per pixel. Time-lapse imaging of 5 min was acquired at a resolution of 512 × 512 pixels at zoom 1, leading to a field of about 608.3 µm and a linear resolution of 1.19 µm per pixel. Image reconstruction was done by acquiring a set of Z-stacks in the tumor regions at a resolution of 512 × 512 pixels at zoom 1, leading to a field of about 608.3 µm and a linear resolution of 1.19 µm per pixel. The stack step size was 2 µm.

Tumor Volume

Tumor volume was measured *in vivo* at different time points post tumor implantation. The subcutaneous volume was estimated by determining the x, y, and z measurements of the tumor under 2-photon microscope. Tumor volume was calculated assuming an ellipsoid shape, where l is the length, w is the width, and h is the height[37]:

$$V = \frac{4}{3} \cdot \pi \cdot \frac{l}{2} \cdot \frac{\omega}{2} \cdot \frac{h}{2}$$

Two-Photon Imaging Analysis

Data collected *in vivo* and *in vitro* using 2-photon microscopy consisted of 12-bit images. *In vitro* Ca^{2+} imaging was conducted at 70–80% cell confluency. Acquisitions were corrected for motion using NoRMCorre Matlab code[38]. ImageJ (NIH) was used to manually draw regions of interest (ROIs) and extract measurements. These measurements were then analyzed using custom-made Matlab code that computes the fluorescence fluctuation of each cell. Briefly, the raw fluorescent trace, F, of each cell extracted using ImageJ was smoothed by calculating its moving mean over a sliding window of 3 s across the whole trace and the minimum value was determined, F_{min} (unless otherwise mentioned). Then the change of fluorescence over time, ΔF/F, was calculated using the following formula:

$$\frac{\Delta F}{F} = \frac{(F - F_{min})}{F_{min}}$$

Once the fluorescence fluctuation has been calculated, the distribution of the ΔF/F of each region of ineterest (ROI) is computed and fitted with a normal distribution to extract its mean (μ) and standard deviation (std, σ). A threshold is set at $\mu + \sigma$. Segments of traces that are higher than the threshold and longer than 3 s are considered as events. Two events are considered discrete if they are > 1 s apart, otherwise they are merged. Duration is defined as time over the threshold. Frequency refers to the number of events per duration of acquisition in each cell.

Pearson's correlation analysis was performed on calcium traces to evaluate how similar the 2 traces were on a temporal scale. This analysis was done on every possible unique pair of calcium traces (ie, unique pairs of cells) in an acquisition field. Therefore, the total number of pairs (counts) is given by the following equation:

$$\text{Total number of pairs} = \sum_{i=1}^{N} \frac{x_i\,(x_i - 1)}{2}$$

where x_i = the number of traces for the i^{th} field of acquisition and N = the number of acquired fields. A permutation test was computed to evaluate the temporal dependency of $[Ca^{2+}]_i$ transients while maintaining its temporal structure. It is done as a resampling-based method, where calcium traces were permutated at random positions on a temporal scale. Briefly, a random number between 0 and 1 was generated and multiplied with the total duration of the trace. Then, the trace is disconnected at the computed random time point and flipped, where this random time point will be the new origin.

Immunohistochemical Analysis

Animals were deeply anesthetized with urethane and perfused transcardially with 4% paraformaldehyde (PFA)/PBS (4% PFA). Samples were post fixed overnight in 4% PFA. For immunofluorescence, brains were sectioned at 60 µm thickness on a vibratome (Leica VT1000 S). Slices were processed as free-floating sections and stained with Hoechst for nuclei labeling (1:500; catalog number: B#2883; Sigma Aldrich) and Ki67 antibody (1:100; Abcam), as a marker of proliferation. Secondary immunostaining was performed using a biotinylated secondary antibody (Anti-rabbit, Vector Lab USA, BA-1000) followed by Alexa 405 streptavidin dye (1:100; Sigma Aldrich). Density counts of Hoechst and Ki67 positive cells were done using the cell counter plug-in (ImageJ) and normalized to its area.

Confocal Image Acquisition of Brain Slices

Fixed tissue was imaged with the Zeiss LSM-900 Airyscan confocal microscope with 405/488/561/640 nm lasers according to the secondary antibody. Images were acquired using a 40× oil immersion objective (NA 1.3). Representative fields were imaged by acquiring a set of Z-stacks (40 µm thick) for each experimental condition. The Z-stacks were collapsed with a maximum intensity projection to a 2D representation.

Statistics

Data were placed in Origin Pro 9.0 to generate graphs. Where appropriate, data have been represented as box plots. Boxes indicate the 25 and 75 percentiles, while whiskers indicate the 5 and 95 percentiles. All data were analyzed using the nonparametric Mann-Whitney test except for the *in vitro* proliferation assay, where the *P*-value was obtained using 2-way ANOVA.

Results

Mouse Model: Creation and Validation

We have stably transfected a murine GB cell line[39] by electroporating GL261-WT cells with a plasmid construct containing a calcium sensor, GCaMP6s, and a RFP, DsRed2, which is modified with the actin-staining peptide, LifeAct (Figure 1a and b). The transfected cells (GL261-TF) allow for the simultaneous assessment of $[Ca^{2+}]_i$ activity and cellular morphology (Figure 1c).

To validate this cell line, we initially examined the *in vitro* proliferation potential of both GL261-WT and GL261-TF cells and found no statistically significant differences (Figure 1d). However, the measure of aspect ratio[40] (Figure 1e) revealed some morphological changes since the GL261-WT cells harbor a more elongated shape compared to the GL261-TF line. Given that elongation is associated with the migratory behavior by modulating traction forces at the cell front and rear,[41] we investigated the difference in their *in vitro* migrational ability by performing a wound healing assay (see Methods) on a confluent cell monolayer. Figure 1f and g shows that the GL261-TF cell line exhibits a reduced migrational potential with 48% closure in 48 h, while GL261-WT cells achieved 100% closure. This difference is mirrored by reduced elongation of the GL261-TF cells during the invasion of the wound (Supplementary Figure 1). The observed discrepancies may be attributed to either the sorting technique used on the transfected cell line, where only a subpopulation of cells was harvested and maintained, and/or to the buffering effects of the Ca^{2+} sensor.[42]

For further analysis, *in vivo* validation was conducted to ensure that the GL261-TF cell line maintains a pathological phenotype upon transplant into the mouse brain. We measured *in vivo* tumor volume in mice implanted with GL261-TF cells to approximate the tumor growth rate. Tumor volume was estimated in mice with an implanted chronic window by 2-photon imaging at different temporal points (Figure 1h, see Methods[37]). The tumor mass was fairly large by the fourth week post implantation, confirming the validity of our fluorescent mouse model as a fast-growing and aggressive tumor (Figure 1i). Indeed, the overall survival of mice bearing either cell line showed no significant difference (Figure 1j), which is consistent with the study done by Pérez et al.,[43] where the median survival of mice transplanted with GL261-WT mice was 39 days. Furthermore, IHC analysis using Hoechst for nuclear staining and Ki67 as a proliferation marker showed no significant differences between GL261-WT and GL261-TF (Supplementary Figure 2).

Heterogenous Morphology of GB Cells

In vivo 2-photon imaging on GL261 tumor revealed 2 distinct tumor regions composed of a primary core mass (TC) and cell streams protruding away from the core formed by cells that migrate into the surrounding brain tissue. The cells populating these territories are characterized by different morphologies, with dense spherical cells in the TC and sparse elongated cells at the periphery. This morphological heterogeneity is different from the predominantly rounded shape observed in *in vitro* GL261 cells (Figure 2a). This observation highlights the crucial role of the surrounding microenvironment in influencing cellular morphology, especially when this feature is predictive of the level of tumorigenicity and metastasis.[44,45] Figure 2b and c provides a quantified representation of these observed morphological differences.

Spontaneous Intracellular Calcium Activity

Next, we investigated spontaneous $[Ca^{2+}]_i$ fluctuations in both regions of the tumor between 11 and 28 days post implantation, as our data indicated no notable differences in global $[Ca^{2+}]_i$ activity within these timeframe (Supplementary Figure 4). Figure 3a and b shows exemplificative $[Ca^{2+}]_i$ activity of cells belonging to the TC and periphery. Imaging was performed for a period of 10 min and we observed vastly different dynamics in these 2 regions (Supplementary Movie 1). Cells located at the TC exhibited only small and sparse $[Ca^{2+}]_i$ events, while cells in the periphery displayed frequent and repetitive $[Ca^{2+}]_i$ transients. This distinction is readily apparent when examining the 2 raster plots obtained for cells belonging to the core or the periphery (bottom left and right of Figure 3a and b).

To analyze this distinctive pattern of $[Ca^{2+}]_i$ transients, we first quantified the percentage of active cells within different territories of the tumor and we compared it with that of cultured GL261-TF cells (Figure 3c). Active cells are defined as cells exhibiting $[Ca^{2+}]_i$ transients exceeding a threshold of $\mu + \sigma$, as determined from the distribution of fluorescence fluctuations, with a frequency of at least 0.0017 Hz [1 event per acquisition period (10 min)]. Our data indicate a higher proportion of active cells is in the peripheral region compared to the tumor mass, whereas in the *in vitro* setting, cells exhibit an intermediary level of activity. The analysis of $[Ca^{2+}]_i$ dynamics revealed that these events are more frequent and shorter in duration in the periphery than in the

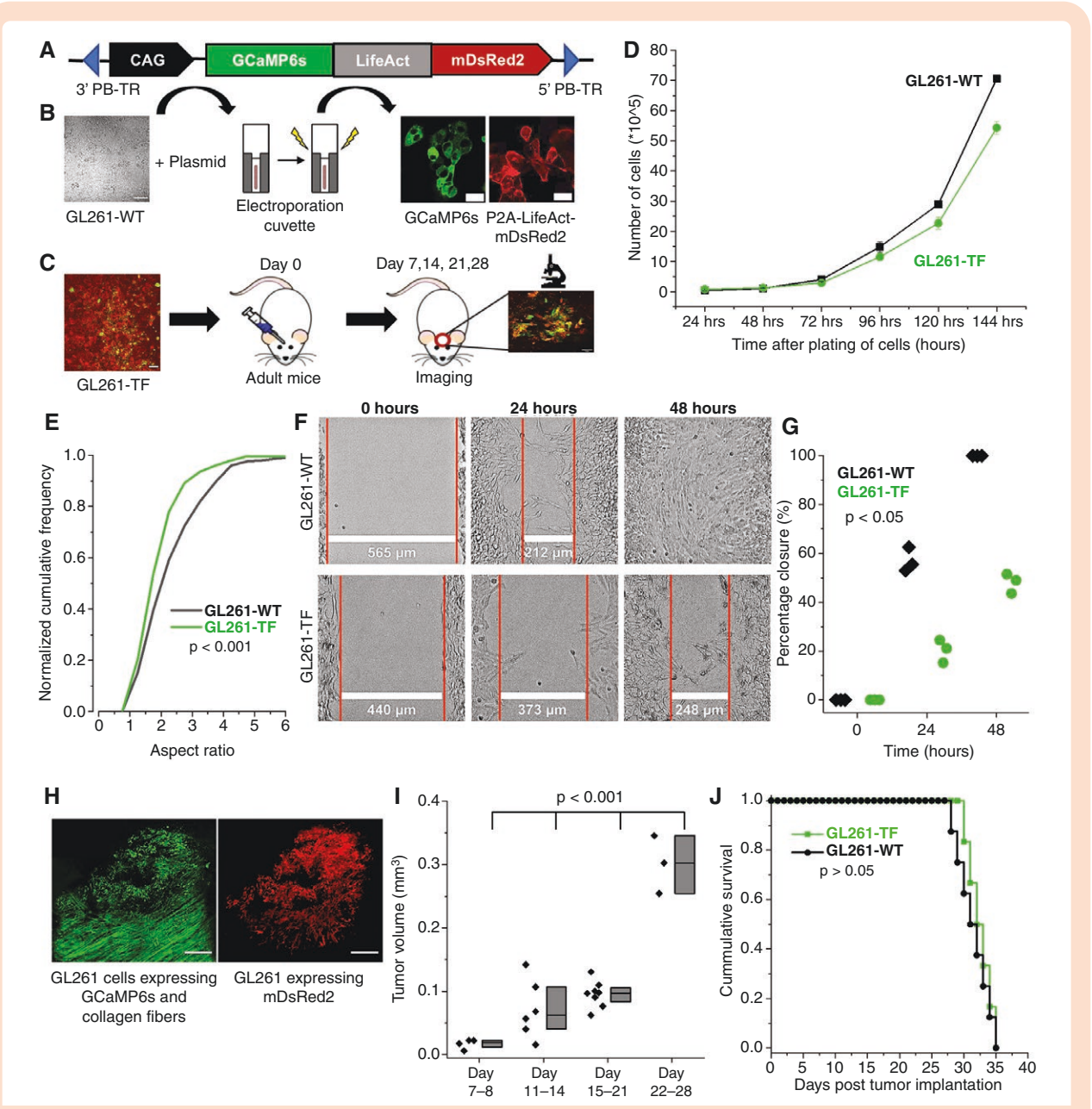

Figure 1. **GL261 fluorescent mouse model. (a)** Plasmid construct with CAG promoter expressing GCaMP6s (green) and LifeAct-DsRed2 (red). **(b)** GL261-WT cell transfection with plasmid generates a fluorescent cell line (GL261-TF) (scale bar: 50 µm). **(c)** Stereotactic intracerebral injection of tumor cells in adult mice (P90-150) and *in vivo* 2-photon imaging. **(d)** *In vitro* proliferation assay. *P*-values were determined by 2-way ANOVA and were not statistically significant ($P = 0.149$; $n = 4$ repetitions). The standard deviation is within the sample size. **(e)** *In vitro* cell morphology (25 cells, $n = 3$ plates/experimental group). **(f)** Wound healing assay. Brightfield imaging on wounded cell plates performed over 48 h ($n = 3$ plates/experimental group). **(g)** Rate of wound closure. **(h)** Mosaic image obtained *in vivo* at the 2-photon microscope showing entire tumor area 8 days post implantation. Maximum projection of a stack imaged every 5 µm from the surface down to about 250 µm depth (scale bar 100 µm). Collagen fibers can be seen as a result of second harmonic generation (SHG). **(i)** GL261-TF tumor growth rate. A total of 11 mice were used to estimate tumor volume, where some mice were chronically imaged at different times. **(j)** Kaplan-Meier survival curve of mice bearing wild type and fluorescent GL261 tumor ($P > .05$; $n = 6$ mice/group). *P*-values in **e, g, i,** and **j** are determined by Mann-Whitney test.

TC. Intriguingly, the temporal characteristics of $[Ca^{2+}]_i$ activity in cultured cells do not reflect that of the periphery or of the TC (Figure 3d-f). These data highlight the influential role of the microenvironment in shaping the tumor signaling pattern. Thus, we hypothesize that cells along the tumor's invading front have increased active $[Ca^{2+}]_i$ activity contributing to an infiltrative phenotype.

Clustered Ca^{2+} Bursts in the Peripheral Region of the GL261 Tumor

The intense $[Ca^{2+}]_i$ activity observed in the peripheral region of the GL261-TF tumor, is also characterized by a notable synchronization of Ca^{2+} bursts within cellular ensembles (Figure 4a). The temporal evolution of a representative

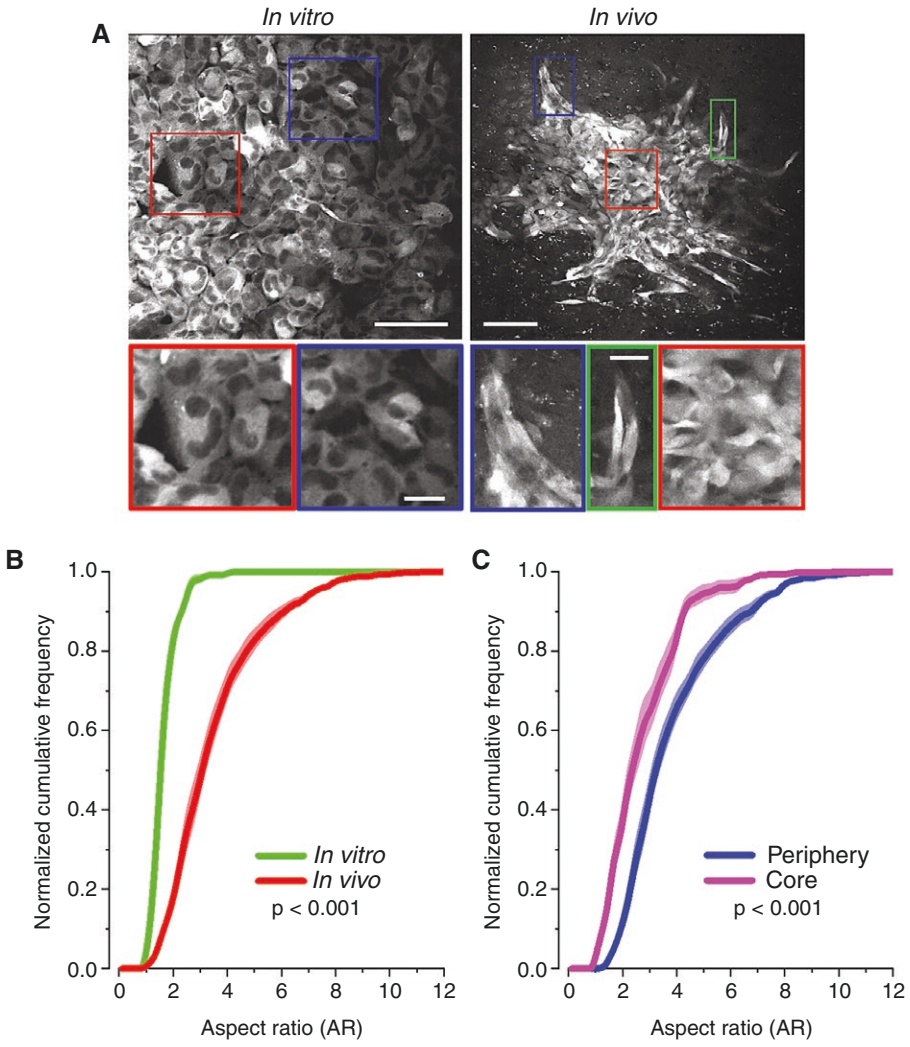

Figure 2. **Morphology of GL261 cells *in vitro* and *in vivo*. (a)** *Left*: Maximum projection of a z-stack of cultured GL261 cells at 80% confluency (6 µm depth and 2 µm step size, calibration bar 100 µm). The cells exhibit a uniform circular morphology (red and blue inset, calibration bar 20 µm). *Right*: Maximum projection of z-stack images 7 days after tumor graft (100 µm depth and 2 µm step size, calibration bar 100 µm). The tumor shows 2 different territories. Near the center, cell density is very high, and cells are more spheroidal (see red inset). At the edges of the tumor, cells are very elongated and arranged in linear chains (green and blue insets, calibration bar 20 µm). **(b and c)** Comparison of cellular morphology using aspect ratio as a parameter. Distributions in **b** show the differences between the cell morphology *in vitro* and *in vivo*, while the distributions in **c** display the aspect ratio measured in the core and periphery of the grafted tumor. The standard error of the mean (SEM) is represented with a shaded area and is within the sample size. Statistical significance determined by the Kolmogorov-Smirnov test (*in vitro*: 5 plates, n = 102 cells; *in vivo*: 788 cells from the peripheral region and 247 cells from the tumor core, data pooled from 8 mice).

data set (white box) is shown in Figure 4b. Figure 4c shows the $[Ca^{2+}]_i$ dynamics of cells encompassing 4 different clusters that exhibit a high degree of inter-cluster synchronization. Correlated activity is quantified by the computation of Pearson's correlation for all possible pairs of $[Ca^{2+}]_i$ traces, revealing a distribution with a large right tail indicating the presence of highly correlated cell clusters. Pairs of traces with a correlation value of $R \geq 0.9$ are highlighted in the shaded red region (Figure 4d). To establish that the temporal organization of $[Ca^{2+}]_i$ activity is not due to the random over imposition of uncorrelated periodic transients, we performed 1000 cycles of random temporal circular permutations on each of these traces (see Methods for details). The resulting linear correlation of all possible pairs was plotted as an averaged distribution curve (gray shaded area) overlaid on the original correlation distribution in Figure 4d. The disappearance of the right tail and the leftward shift of the curve after permutation shows that the rightmost population is attributable to bona fide correlation. This pronounced coactivation is visually apparent in the connectivity map in Figure 4e, where the red lines join cells with a correlation coefficient $R \geq 0.9$. Finally, we plotted a global distribution of correlation coefficients from 715 cells obtained from 7 mice (11 acquisition fields) (Figure 4f). The strong bias of the distribution toward the right supports our observation of high synchronization in ensembles of cell located at the peripheral region of the tumor (Supplementary Figure 5A).

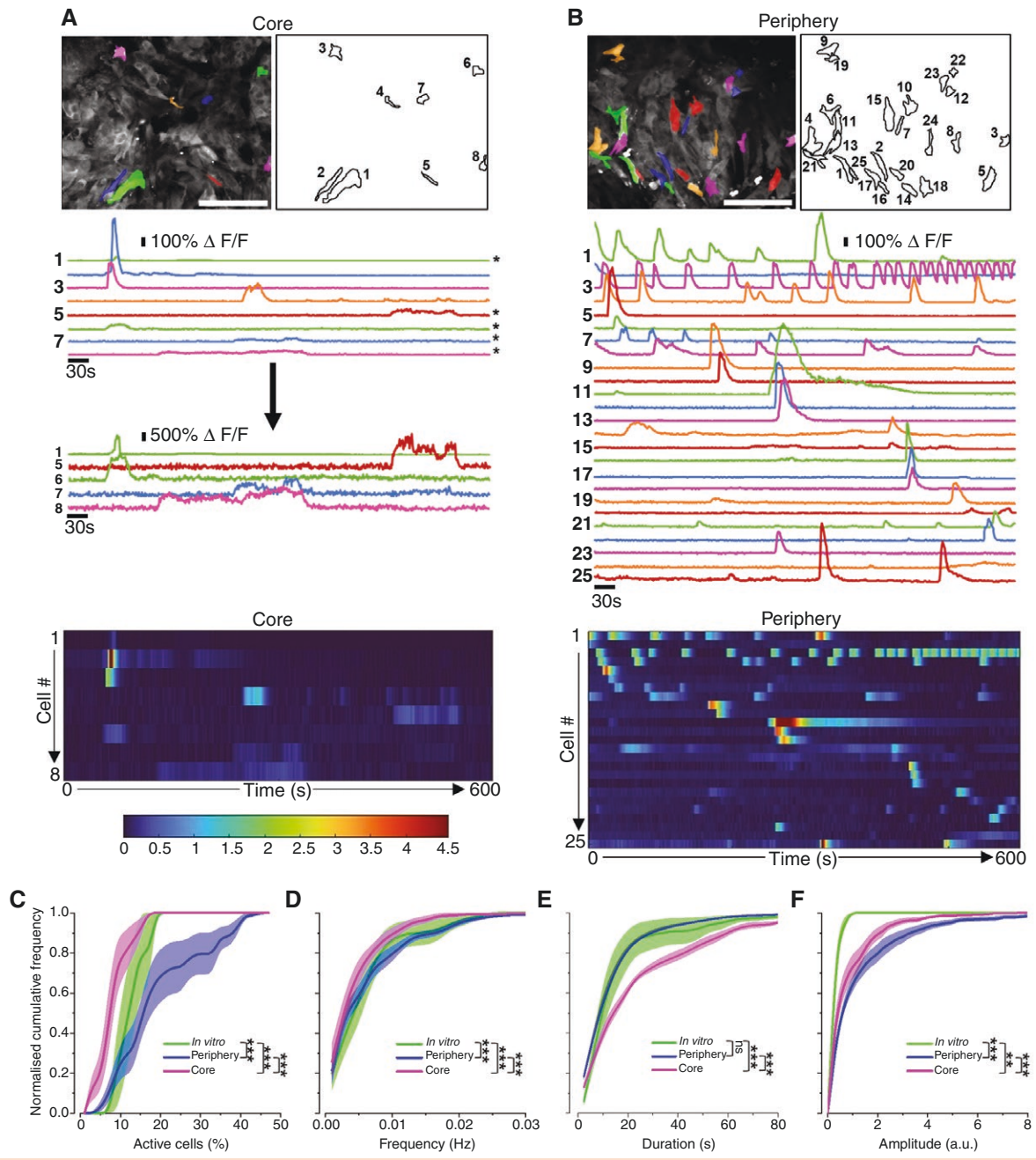

Figure 3. **Morphology of $[Ca^{2+}]i$ events in the core and periphery of the tumor and quantification of $[Ca^{2+}]i$ dynamics *in vitro* and *in vivo*. (a and b)** *Top*: Illustration of cellular locations. The color of each indicated cell corresponds to the traces below. The images are the maximum projection of a 10-min movie sequence with a sampling period of 1.07 s (scale bar 100 μm). *Middle*: Individual Ca^{2+} traces presented as changes in fluorescence intensity (ΔF/F) stacked according to cell ID. In panel **a**, Ca^{2+} traces of some cells located at the tumor core (marked with asterisks) were amplified by a factor of 5 to enhance the visibility of their activity. *Bottom*: Raster plot of GCaMP6s ΔF/F of individual cells. **(c)** Percentage of active cells. This analysis was measured over 43 fields at the peripheral region, 25 fields at tumor mass, and 5 GL261-TF culture plates. **(d, e, and f)** Representation of the frequency, duration, and amplitude of $[Ca^{2+}]_i$ events. Shaded areas represent the standard error of the mean. A total of 8 mice were used and results represent pooled data from cells that were imaged from day 11 to day 28 post tumor implantation (788 cells in the peripheral region and 247 cells in the tumor mass). Quantification on culture plates was done at 80-90% confluency (n = 5 plates). Statistical significance determined by Kolmogorov-Smirnov test (***P < .001, **P < .01, ns P > .05).

Short-Term Migration Pattern of the GL261T

Next, we examined the putative correlation of $[Ca^{2+}]_i$ activity with the migrational potential of the GL261 cells. We employed time-lapse imaging at 1 Hz resolution to measure the position of cells together with Ca^{2+} imaging. The trajectory of each cell is plotted by assuming as reference its coordinate at time 0. (Figure 5a-c). We found that

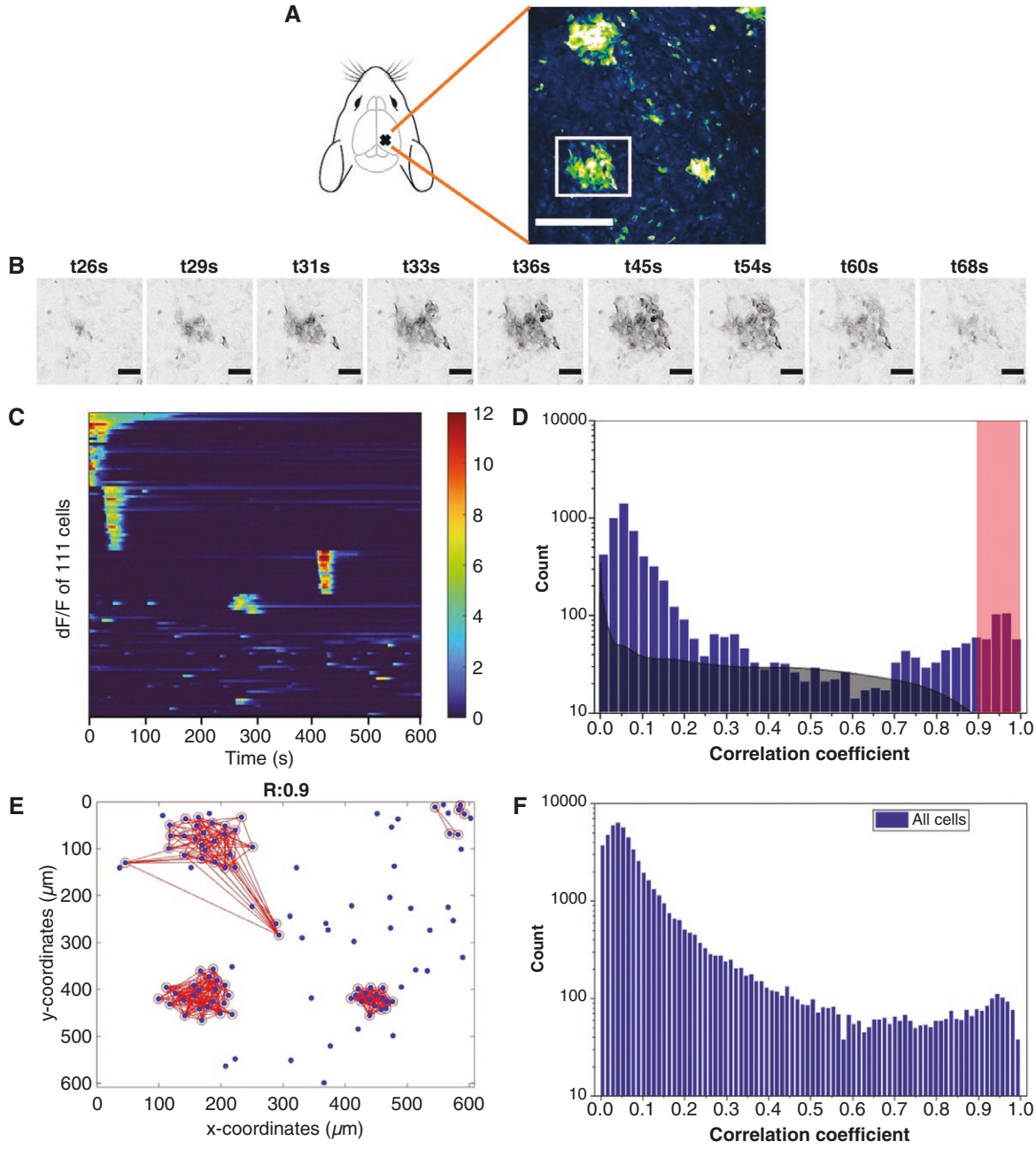

Figure 4. **Synchronized $[Ca^{2+}]_i$ bursts in the GL261 tumor. (a)** Intravital 2-photon calcium imaging of a tumor 18 days post implantation. Image on the right represents the standard deviation projection of a 10-min movie sequence, 80 μm depth from the surface (scale bar: 200 μm). **(b)** Temporal evolution of $[Ca^{2+}]_i$ transients of a selected cell cluster represented by the white square in **a** (time in seconds) (scale bar: 50 μm). **(c)** Raster plot corresponding to ΔF/F of 111 cells belonging to clusters and remote cells. ROIs from clusters were grouped together manually by the experimenter in the plot for better visualization of ΔF/F activation. **(d)** Distribution of Pearson's correlation coefficient of $[Ca^{2+}]_i$ computed on pairs of traces (blue bars). The distribution curve represented by the gray shaded area shows the paired correlation of traces after permutation. Data that fall in the red-shaded area represents pairs of traces that have a correlation of R ≥ 0.9. **(e)** Functional connectivity map of cells (red lines) at correlation threshold, R ≥ 0.9. Centroids of all 111 ROIs are represented in blue with spatial coordinates as in the 2-photon imaging field in **a**. **(f)** Distribution of correlation coefficients of $[Ca^{2+}]_i$ traces of 715 cells obtained from 7 mice.

the cellular clusters that exhibit high temporal synchronization appear to be formed by cells that migrate with a common directional bias (Figure 5c). In contrast, cells not belonging to any functional Ca^{2+} cluster do not show any directional bias (Figure 5b and Supplementary Figure 5B).

Then we analyzed migration by time-lapse imaging, estimating the accumulated distance traveled in 60 min of cells in the TC and periphery. The displacement of the center of mass of each cell was measured every minute during Ca^{2+} imaging. The trajectories of each cell are illustrated in

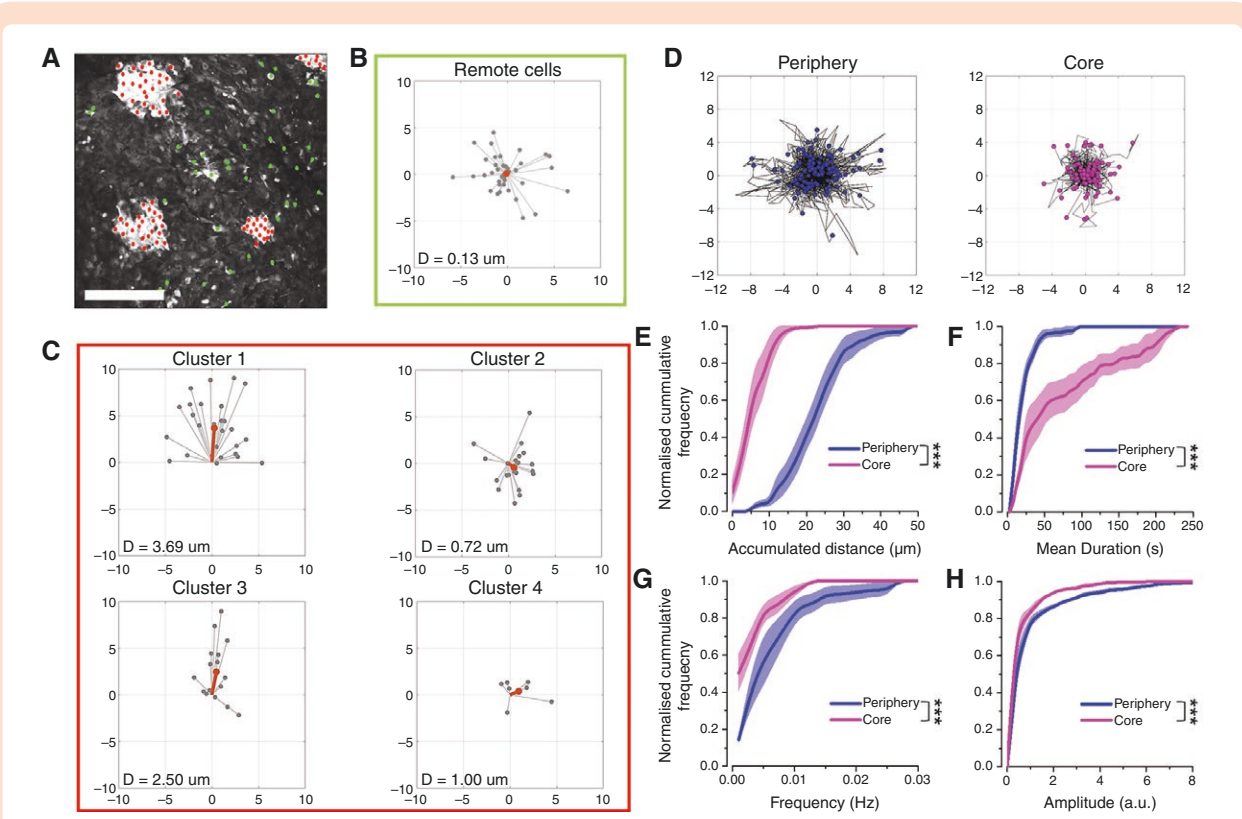

Figure 5. Migrational potential and $[Ca^{2+}]i$ dynamics. (**a**) Two-photon image as in Figure 5a (scale bar: 200 μm). Red dots represent the centroid of cells belonging to clusters, while green dots represent the remote cells as determined by the correlation analysis. (**b and c**) Cellular trajectories of remote cells (green square) and cell clusters (red square quantified in a period of 10 min). Euclidean distances of each cell are represented with a gray marker line and its weighted average is represented by an orange marker line. (Cluster 1: 27 cells; Cluster 2: 23 cells; Cluster 3: 16 cells; Cluster 4: 7 cells; Remote cells: 38 cells) (D = Average Euclidean Distance). (**d**) Representative plots of cellular trajectories in the peripheral region (left) and tumor core (right). (**e**) Quantification of cell motility using accumulated distance as a parameter. The mean velocity of the cells is 0.67 μm/min at the peripheral region and 0.20 μm/min at the tumor core. (**f, g, and h**) Intracellular calcium dynamics of migrating cells. Experiments were done on $n = 5$ mice (114 cells at the peripheral region and 98 cells at the tumor core). Statistical significance determined by Kolmogorov-Smirnov test (*** $P < .001$).

Figure 5d. This representation displays the diffusivity of cell tracks, with peripheral cells exhibiting longer trajectories. Cellular motility was quantified by computing the total displacement of these cells (Figure 5e and Supplementary Figure 3), and our findings demonstrate that cells in the periphery travel a larger cumulative distance than cells in the tumor bulk, suggesting increased cellular motility. As noticed above, also in this dataset, we observed that $[Ca^{2+}]_i$ oscillations in the periphery were more frequent with higher amplitude and shorter duration (Figure 5e, g, and h), suggesting a correlation between $[Ca^{2+}]_i$ activity and cellular migration. Collectively, these findings show a correlation between the heterogenous $[Ca^{2+}]_i$ activity and cell migration, thus suggesting a possible role of $[Ca^{2+}]_i$ signaling in GB infiltration.

Discussion

We developed a fluorescent orthotropic GB model expressing a genetically encoded calcium sensor and exploited time-lapse *in vivo* microscopy to analyze intrinsic $[Ca^{2+}]_i$ dynamics and its correlation with tumor cell migration on a short temporal scale.

First, we validated our fluorescent murine model to examine the effect of transfection, cell sorting, and the expression of GCaMP6s-DsRed2 on GL261 cell properties. Even if GL261-TF cells exhibit a less aggressive phenotype *in vitro* compared to control GL261-WT cells, we observed no substantial differences in the survival curves of mice implanted with either cell line (Figure 1). This suggests that both cell lines proliferate similarly within the complex environment of the brain. As a result, the insertion of fluorescent reporters did not alter the *in vivo* growth and aggressive phenotype of the GL261 tumor, in agreement with well-established models described in literature.[46–50] However, it is essential to acknowledge that the GL261 cell line, while commonly used in GB research, demonstrates limited invasive capacity compared to more aggressive patient-derived models. This limitation should be considered when interpreting our results. Despite this, GL261 remains a well-characterized murine model that recapitulates key aspects of human GB, such as aggressive growth, invasion patterns, and response to therapies.[51] The GL261

model carries mutations in the p53 and Pten genes, which are frequently altered in human GB, making it a valuable tool for studying fundamental mechanisms like calcium signaling in a reproducible environment. Future studies using patient-derived xenograft models or human GB stem-like cells could provide a broader perspective on the tumor microenvironment and its relationship to calcium signaling. Although differences in calcium signaling heterogeneity between GL261 and human tumors remain to be explored, recent studies suggest that murine models can offer insights into the mechanisms of tumor progression, while still requiring validation with human models for translational purposes.

Cellular morphology provides valuable information of cellular state and physiology. Cells change their shape when influenced by their external environment and physiological state.[52,53] In our model, we found that cultured GL261 cells seem to have a homogenous cellular morphology with a low aspect ratio. However, when they are subjected to a directional cell migration assay *in vitro*, that is wound healing assay, these morphologically homogenous cells develop a more polarized phenotype as they migrate to close the wound (Supplementary Figure 1). Indeed, we observed similar characteristics *in vivo* where GL261 cells develop different morphological phenotypes depending on their location within the tumor. GL261 cells at the invading region of the tumor exhibit an elongated morphology compared to the rounded-shaped cells in the TC. This demonstrates the importance of the interaction between tumor cells and the host environment for malignant development, progression as well as cancer cell state.[54,55]

This dual morphological feature of our GL261 cells led us to further investigate the potential differences in cellular signaling, as the signaling landscape of a cell is bidirectionally linked to its morphology.[52] Our data revealed an increased $[Ca^{2+}]_i$ activity in GL261 cells located at the borders of the tumor compared to the core suggesting that peripheral tumor cells utilize short and frequent $[Ca^{2+}]_i$ transients to establish a communication network facilitating an infiltrative phenotype. This aligns with studies highlighting the role of calcium signaling in cancer cell communication and invasion.[21,56,57] Moreover, our data highlight the importance of the complex environment of the brain in inducing heterogeneous interactions that alter tumor intracellular signaling thus facilitating necessary adaptation for infiltration and metastasis.[58,59] This can be seen clearly from the $[Ca^{2+}]_i$ activity of cultured GL261 cells where the cells are substantially less active (Figure 3), further proving that the bidimensional environment of an *in vitro* setting does not resemble the heterogeneity of *in vivo* systems.

Another feature that emerged from our data is the presence of synchronized $[Ca^{2+}]_i$ bursts within clusters of peripheral GL261 tumor cells. In an attempt to understand the modulation of $[Ca^{2+}]_i$ activity, Venkatesh et al. [10] and Venkataramani et al. [9] studied functional neuroglioma interactions and observed synchronized patterns of Ca^{2+} activity in connected human glioma cells when neurons expressing channel-rhodopsin were stimulated.[9,10] In addition to this, Hausmann et al. also reported similar features of rhythmic Ca^{2+} oscillations in primary human GB model.[11] However, similar activity patterns were never reported in murine GB models. Our study discloses the presence of autonomous synchronization of $[Ca^{2+}]_i$ activity in clusters of tumor cells thus suggesting the ability of this murine model to recapitulate characteristics of human GB.

Finally, we studied the motility of malignant cells by comparing the total distance traveled by tumor cells at the 2 defined regions and their $[Ca^{2+}]_i$ activity. Interestingly, we found that cells located at the periphery had increased cellular motility and exhibited more frequent $[Ca^{2+}]_i$ signaling compared to the cells at the tumor bulk. This highlights the potential significance of intracellular Ca^{2+} oscillations within distinct locations of the tumor, notably in terms of frequency and duration, in composing a specific role of $[Ca^{2+}]_i$ dynamics for tumor cell proliferation and migration.[60,61] In addition to this, we also demonstrated that cells belonging to the highly synchronized clusters display a bias in their migratory direction, suggesting a potential mechanism for collective cell invasion in GB.

Our work provides insight on the complex interplay between intracellular calcium dynamics and cellular motility in GB, emphasizing the significance of intratumoral signaling in tumor progression *in vivo*. A comparative review of Ca^{2+} signaling in cancer-derived cells versus non-cancer cells reveals significant remodeling of Ca^{2+} homeostasis in tumors.[62] These changes often manifest in alterations such as enhanced Ca^{2+} influx or differences in the recovery rates of intracellular Ca^{2+} levels after stimulation. Such findings suggest that Ca^{2+} signaling pathways may be specifically adapted in cancer cells to support malignancy. For instance, Ca^{2+} involvement in processes such as cell proliferation, migration, and invasion has been widely reported.[63,64] Furthermore, studies have shown that Ca^{2+} signaling inhibitors can reduce GB cell invasiveness and alter the tumor microenvironment.[24,65] These findings align with the increased Ca^{2+} signaling activity observed in the tumor periphery in our study and suggest that modulating calcium dynamics could impair cellular crosstalk and tumor expansion. Future studies should focus on elucidating the molecular mechanisms governing $[Ca^{2+}]_i$ signaling in GB and exploring its therapeutic implications. Targeting aberrant $[Ca^{2+}]_i$ activity may represent a promising strategy for inhibiting GB invasion and improving patient outcomes.

Supplementary Material

Supplementary material is available online at *Neuro-Oncology Advances* (https://academic.oup.com/noa).

Keywords:

calcium imaging | glioblastoma | intravital 2-photon imaging | tumor heterogeneity

LAY SUMMARY

Glioblastoma (GBM) is an aggressive brain cancer that is difficult to treat. Calcium is an important ion that helps cells function.

The authors of this study wanted to see if calcium levels changed across a tumor. To do this, they used special imaging techniques to look at calcium levels in GBM cells from different areas of the tumor. Their study found that cells in the center of the tumor had low calcium activity and moved less, while cells at the edges had higher calcium activity and moved more.

Funding

This work was supported by NEXTGENERATIONEU (NGEU) and funded by the Ministry of University and Research (MUR), National Recovery and Resilience Plan (NRRP), project MNESYS (PE0000006) - a multiscale integrated approach to the study of the nervous system in health and disease (DN. 1553 11.10.2022).

Acknowledgments

We would like to thank Silvia Burchielli, Cecilia Ciampi, Sara Ciampi, and Francesca Biondi for their technical help in animal care.

Conflict of interest statement

The authors have declared that no conflict of interests exists.

Authorship statement

Design of the project: G.M.R., V.P., E.P. Production of stable cell line: V.P., E.P., F.T., R.P. *In vitro* study: V.P. *In vivo* imaging: V.P., E.P., S.L., G.M.R. Analyses: V.P., G.M.R. Computer coding: V.P. Immunohistochemistry: V.P., S.L. Figure preparation: V.P., S.L., G.M.R. Writing manuscript: V.P., S.L., G.M.R. All authors reviewed the final manuscript.

Data availability

All data will be made available upon reasonable request.

Affiliations

National Enterprise for Nanoscience and Nanotechnology (NEST), Istituto Nanoscienze Consiglio Nazionale delle Ricerche (CNR) and Scuola Normale Superiore, Pisa, Italy (V.P., E.P., F.T., R.P., S.L., G.M.R.); Institute of Neuroscience CNR, Pisa, Italy (V.P., S.L.); Institute of Biophysics CNR, Pisa, Italy (G.M.R.)

References

1. Bai J, Varghese J, Jain R. Adult glioma WHO classification update, genomics, and imaging: what the radiologists need to know. *Top Magn Reson Imaging*. 2020;29(2):71–82.
2. Louis DN, Wesseling P, Aldape K, et al. cIMPACT-NOW update 6: new entity and diagnostic principle recommendations of the cIMPACT-Utrecht meeting on future CNS tumor classification and grading. *Brain Pathol*. 2020;30(4):844–856.
3. Nørøxe DS, Poulsen HS, Lassen U. Hallmarks of glioblastoma: a systematic review. *ESMO Open*. 2016;1(6):e000144.
4. Preusser M, De Ribaupierre S, Wöhrer A, et al. Current concepts and management of glioblastoma. *Ann Neurol*. 2011;70(1):9–21.
5. G. Gritsenko P, Ilina O, Friedl P. Interstitial guidance of cancer invasion. *J Pathol*. 2012;226(2):185–199.
6. Yekula A, Yekula A, Muralidharan K, et al. Extracellular vesicles in glioblastoma tumor microenvironment. *Front Immunol*. 2020;10:3137.
7. Osswald M, Jung E, Sahm F, et al. Brain tumour cells interconnect to a functional and resistant network. *Nature*. 2015;528(7580):93–98.
8. Winkler F, Wick W. Harmful networks in the brain and beyond. *Science*. 2018;359(6380):1100–1101.
9. Venkataramani V, Tanev DI, Strahle C, et al. Glutamatergic synaptic input to glioma cells drives brain tumour progression. *Nature*. 2019;573(7775):532–538.
10. Venkatesh HS, Morishita W, Geraghty AC, et al. Electrical and synaptic integration of glioma into neural circuits. *Nature*. 2019;573(7775):539–545.
11. Hausmann D, Hoffmann DC, Venkataramani V, et al. Autonomous rhythmic activity in glioma networks drives brain tumour growth. *Nature*. 2023;613(7942):179–186.
12. Berridge MJ, Lipp P, Bootman MD. The versatility and universality of calcium signalling. *Nat Rev Mol Cell Biol*. 2000;1(1):11–21.
13. Berridge MJ, Bootman MD, Roderick HL. Calcium signalling: dynamics, homeostasis and remodelling. *Nat Rev Mol Cell Biol*. 2003;4(7):517–529.
14. Clapham DE. Calcium signaling. *Cell*. 2007;131(6):1047–1058.
15. Zündorf G, Reiser G. Calcium dysregulation and homeostasis of neural calcium in the molecular mechanisms of neurodegenerative diseases provide multiple targets for neuroprotection. *Antioxid Redox Signal*. 2011;14(7):1275–1288.
16. Rosenberg SS, Spitzer NC. Calcium signaling in neuronal development. *Cold Spring Harb Perspect Biol*. 2011;3(10):a004259.
17. Burgoyne RD, Haynes LP. Understanding the physiological roles of the neuronal calcium sensor proteins. *Mol Brain*. 2012;5(1):2.
18. Mathur R, Wang Q, Schupp PG, et al. Glioblastoma evolution and heterogeneity from a 3D whole-tumor perspective. *Cell*. 2024;187(2):446–463.e16.
19. Cuddapah VA, Sontheimer H. Ion channels and transporters [corrected] in cancer. 2. Ion channels and the control of cancer cell migration. *Am J Physiol Cell Physiol*. 2011;301(3):C541–C549.
20. Nimmrich V, Gross G. P/Q-type calcium channel modulators. *Br J Pharmacol*. 2012;167(4):741–759.
21. Zhang Y, Zhang J, Jiang D, et al. Inhibition of T-type Ca2+ channels by endostatin attenuates human glioblastoma cell proliferation and migration. *Br J Pharmacol*. 2012;166(4):1247–1260.
22. Visa A, Sallán MC, Maiques O, et al. T-type Cav3. 1 channels mediate progression and chemotherapeutic resistance in glioblastoma. *Cancer Res*. 2019;79(8):1857–1868.
23. Valerie NCK, Dziegielewska B, Hosing AS, et al. Inhibition of T-type calcium channels disrupts Akt signaling and promotes apoptosis in glioblastoma cells. *Biochem Pharmacol*. 2013;85(7):888–897.

24. Zhang Y, Cruickshanks N, Yuan F, et al. Targetable T-type calcium channels drive glioblastoma. *Cancer Res.* 2017;77(13):3479–3490.
25. Amantini C, Mosca M, Nabissi M, et al. Capsaicin-induced apoptosis of glioma cells is mediated by TRPV1 vanilloid receptor and requires p38 MAPK activation. *J Neurochem.* 2007;102(3):977–990.
26. Stock K, Kumar J, Synowitz M, et al. Neural precursor cells induce cell death of high-grade astrocytomas through stimulation of TRPV1. *Nat Med.* 2012;18(8):1232–1238.
27. Nabissi M, Morelli MB, Santoni M, Santoni G. Triggering of the TRPV2 channel by cannabidiol sensitizes glioblastoma cells to cytotoxic chemotherapeutic agents. *Carcinogenesis.* 2013;34(1):48–57.
28. Nabissi M, Morelli MB, Amantini C, et al. TRPV2 channel negatively controls glioma cell proliferation and resistance to Fas-induced apoptosis in ERK-dependent manner. *Carcinogenesis.* 2010;31(5):794–803.
29. Alptekin M, Eroglu S, Tutar E, et al. Gene expressions of TRP channels in glioblastoma multiforme and relation with survival. *Tumour Biol.* 2015;36(12):9209–9213.
30. Wondergem R, Bartley JW. Menthol increases human glioblastoma intracellular Ca 2+, BK channel activity and cell migration. *J Biomed Sci.* 2009;16(1):90.
31. Leng TD, Li MH, Shen JF, et al. Suppression of TRPM 7 inhibits proliferation, migration, and invasion of malignant human glioma cells. *CNS Neurosci Ther.* 2015;21(3):252–261.
32. Burnstock G, Di Virgilio F. Purinergic signalling and cancer. *Purinergic Signal.* 2013;9(4):491–540.
33. Wei W, Ryu JK, Choi HB, McLarnon JG. Expression and function of the P2X7 receptor in rat C6 glioma cells. *Cancer Lett.* 2008;260(1-2):79–87.
34. Fang J, Chen X, Zhang L, et al. P2X7R suppression promotes glioma growth through epidermal growth factor receptor signal pathway. *Int J Biochem Cell Biol.* 2013;45(6):1109–1120.
35. Gehring MP, Kipper F, Nicoletti NF, et al. P2X7 receptor as predictor gene for glioma radiosensitivity and median survival. *Int J Biochem Cell Biol.* 2015;68:92–100.
36. Vannini E, Maltese F, Olimpico F, et al. Progression of motor deficits in glioma-bearing mice: Impact of CNF1 therapy at symptomatic stages. *Oncotarget.* 2017;8(14):23539–23550.
37. Sápi J, Kovács L, Drexler DA, et al. Tumor volume estimation and quasi-continuous administration for most effective bevacizumab therapy. *PLoS One.* 2015;10(11):e0142190.
38. Pnevmatikakis EA, Giovannucci A. NoRMCorre: An online algorithm for piecewise rigid motion correction of calcium imaging data. *J Neurosci Methods.* 2017;291:83–94.
39. Haddad AF, Young JS, Amara D, et al. Mouse models of glioblastoma for the evaluation of novel therapeutic strategies. *Neurooncol Adv.* 2021;3(1):vdab100.
40. Moncayo G, Grzmil M, Smirnova T, et al. SYK inhibition blocks proliferation and migration of glioma cells and modifies the tumor microenvironment. *Neuro Oncol.* 2018;20(5):621–631.
41. Zhong Y, Ji B. Impact of cell shape on cell migration behavior on elastic substrate. *Biofabrication.* 2013;5(1):015011.
42. McMahon SM, Jackson MB. An inconvenient truth: calcium sensors are calcium buffers. *Trends Neurosci.* 2018;41(12):880–884.
43. Pérez JE, Kopecky J, Visse E, Darabi A, Siesjö P. Convection-enhanced delivery of temozolomide and whole cell tumor immunizations in GL261 and KR158 experimental mouse gliomas. *BMC Cancer.* 2020;20(1):1–12.
44. Wolfenson H, Yang B, Sheetz MP. Steps in mechanotransduction pathways that control cell morphology. *Annu Rev Physiol.* 2019;81:585–605.
45. Conner S, Guarin JR, Le TT, et al. Cell morphology best predicts tumorigenicity and metastasis in vivo across multiple TNBC cell lines of different metastatic potential. *bioRxiv.* Published online June 14, 2023. doi:10.1101/2023.06.14.544969
46. Newcomb EW, Zagzag D. The murine GL261 glioma experimental model to assess novel brain tumor treatments. *CNS Cancer.* 2009:227–241.
47. Jin F, Jin-Lee H, Johnson A. Mouse models of experimental glioblastoma. *Exon Publications.* 2021:15–45.
48. Costa B, Fletcher MNC, Boskovic P, et al. A set of cell lines derived from a genetic murine glioblastoma model recapitulates molecular and morphological characteristics of human tumors. *Cancers (Basel).* 2021;13(2):230.
49. Candolfi M, Curtin JF, Nichols WS, et al. Intracranial glioblastoma models in preclinical neuro-oncology: neuropathological characterization and tumor progression. *J Neurooncol.* 2007;85(2):133–148.
50. Szatmári T, Lumniczky K, Désaknai S, et al. Detailed characterization of the mouse glioma 261 tumor model for experimental glioblastoma therapy. *Cancer Sci.* 2006;97(6):546–553.
51. Brennan CW, Verhaak RGW, McKenna A, et al; TCGA Research Network. The somatic genomic landscape of glioblastoma. *Cell.* 2013;155(2):462–477.
52. Prasad A, Alizadeh E. Cell form and function: interpreting and controlling the shape of adherent cells. *Trends Biotechnol.* 2019;37(4):347–357.
53. Urzì O, Gasparro R, Costanzo E, et al. Three-dimensional cell cultures: The bridge between in vitro and in vivo models. *Int J Mol Sci .* 2023;24(15):12046.
54. Deaglio S, Hartmann TN. The importance of tumor--host interactions in adult B-cell leukemias and lymphomas. *Int J Mol Sci.* 2020;21(18):691.
55. Alizadeh E, Castle J, Quirk A, et al. Cellular morphological features are predictive markers of cancer cell state. *Comput Biol Med.* 2020;126:104044.
56. Maklad A, Sharma A, Azimi I. Calcium signaling in brain cancers: roles and therapeutic targeting. *Cancers (Basel).* 2019;11(2):145.
57. Morrone FB, Gehring MP, Nicoletti NF. Calcium channels and associated receptors in malignant brain tumor therapy. *Mol Pharmacol.* 2016;90(3):403–409.
58. Caruso FP, Garofano L, D'Angelo F, et al. A map of tumor--host interactions in glioma at single-cell resolution. *GigaScience.* 2020;9(10):giaa109.
59. Leiss L, Mutlu E, Rahman MA, Enger PO. Tumor-host interactions in malignant gliomas. *Biomark Tumor Microenviron.* 2017:465–479.
60. Cui C, Merritt R, Fu L, Pan Z. Targeting calcium signaling in cancer therapy. *Acta Pharm Sin B.* 2017;7(1):3–17.
61. Parekh AB. Decoding cytosolic Ca2+ oscillations. *Trends Biochem Sci.* 2011;36(2):78–87.
62. Stewart TA, Yapa KTDS, Monteith GR. Altered calcium signaling in cancer cells. *Biochim Biophys Acta.* 2015;1848(10):2502–2511.
63. Roderick HL, Cook SJ. Ca2+ signalling checkpoints in cancer: remodelling Ca2+ for cancer cell proliferation and survival. *Nat Rev Cancer.* 2008;8(5):361–375.
64. Prevarskaya N, Skryma R, Shuba Y. Calcium in tumour metastasis: new roles for known actors. *Nat Rev Cancer.* 2011;11(8):609–618.
65. Monteith GR, Prevarskaya N, Roberts-Thomson SJ. The calcium–cancer signalling nexus. *Nat Rev Cancer.* 2017;17(6):373–380.